**PAPER • OPEN ACCESS**

# Multilayer $WSe_2$/ZnO heterojunctions for self-powered, broadband, and high-speed photodetectors

To cite this article: Hamidreza Ghanbari *et al* 2023 *Nanotechnology* **34** 285207

View the article online for updates and enhancements.

You may also like

- Preparation of carnation-like Ag-ZnO composites for enhanced photocatalysis under visible light
Anh-Tuan Vu, Van Hung Mac, Thanh Hung Nguyen et al.

- Research advances in ZnO nanomaterials-based UV photode tectors: a review
Jinning Hu, Jun Chen, Teng Ma et al.

- Pyro-phototronic nanogenerator based on flexible 2D ZnO/graphene heterojunction and its application in self-powered near infrared photodetector and active analog frequency modulation
Parikshit Sahatiya, Akash Shinde and Sushmee Badhulika

This content was downloaded from IP address 207.23.176.54 on 15/05/2023 at 23:02

OPEN ACCESS
IOP Publishing
Nanotechnology
Nanotechnology **34** (2023) 285207 (11pp)
https://doi.org/10.1088/1361-6528/acca8b

# Multilayer $WSe_2$/ZnO heterojunctions for self-powered, broadband, and high-speed photodetectors

**Hamidreza Ghanbari[1,3], Amin Abnavi[1,3,*], Amirhossein Hasani[1], Fahmid Kabir[1], Ribwar Ahmadi[1], Mohammad Reza Mohammadzadeh[1], Mirette Fawzy[2], Thushani De Silva[1] and Michael M Adachi[1,*]**

[1] School of Engineering Science, Simon Fraser University, 8888 University Drive, Burnaby, British Columbia, V5A 1S6, Canada
[2] Department of Physics, Simon Fraser University, 8888 University Drive, Burnaby, British Columbia, V5A 1S6, Canada

E-mail: Amin_Abnavi@sfu.ca and mmadachi@sfu.ca

Received 26 February 2023, revised 26 March 2023
Accepted for publication 5 April 2023
Published 2 May 2023

**Abstract**
Self-powered broadband photodetectors have attracted great interest due to their applications in biomedical imaging, integrated circuits, wireless communication systems, and optical switches. Recently, significant research is being carried out to develop high-performance self-powered photodetectors based on thin 2D materials and their heterostructures due to their unique optoelectronic properties. Herein, a vertical heterostructure based on p-type 2D $WSe_2$ and n-type thin film ZnO is realized for photodetectors with a broadband response in the wavelength range of 300–850 nm. Due to the formation of a built-in electric field at the $WSe_2$/ZnO interface and the photovoltaic effect, this structure exhibits a rectifying behavior with a maximum photoresponsivity and detectivity of $\sim$131 mA $W^{-1}$ and $\sim 3.92 \times 10^{10}$ Jones, respectively, under an incident light wavelength of $\lambda = 300$ nm at zero voltage bias. It also shows a 3-dB cut-off frequency of $\sim$300 Hz along with a fast response time of $\sim$496 $\mu$s, making it suitable for high-speed self-powered optoelectronic applications. Furthermore, the facilitation of charge collection under reverse voltage bias results in a photoresponsivity as high as $\sim$7160 mA $W^{-1}$ and a large detectivity of $\sim 1.18 \times 10^{11}$ Jones at a bias voltage of $-5$ V. Hence, the p-$WSe_2$/n-ZnO heterojunction is proposed as an excellent candidate for high-performance, self-powered, and broadband photodetectors.

Supplementary material for this article is available online

Keywords: $WSe_2$/ZnO heterojunction, self-powered photodetectors, broadband photodetectors, 2D Materials, vertical heterostructure

(Some figures may appear in colour only in the online journal)

[3] These authors contributed equally to this work.
[*] Authors to whom any correspondence should be addressed.

Original content from this work may be used under the terms of the Creative Commons Attribution 4.0 licence. Any further distribution of this work must maintain attribution to the author(s) and the title of the work, journal citation and DOI.

## 1. Introduction

Photodetectors, which convert incident photons into electrical signals, play an important role in many applications including biological/medical imaging [1], optical telecommunications [2], environmental monitoring [3], astronomical observations [4], and integrated circuits [5]. Traditional photodetectors require an external bias to produce a detectable photocurrent,


© 2023 The Author(s). Published by IOP Publishing Ltd

limiting their performance in terms of dark current [6], circuit noise [7], and power consumption [8]. On the other hand, self-powered photodetectors (SPPDs) can detect the optical signals without applying an external bias voltage based on three mechanisms: (I) photovoltaic effect in the p–n or the Schottky junction-based photodetectors [9, 10]; (II) pyro-phototronic effect in the pyroelectric-based photodetectors [4]; (III) tribo-phototronic effect in the triboelectric nanogenerators [11]. SPPDs have a wide range of applications such as solar cell technology [9], gas sensors [12, 13], and remote sensing [14].

Recently, SPPDs based on 2D transition metal dichalcogenides (TMDs) and their heterostructures have attracted great attention due to their ultrahigh photoresponsivity [15], fast response [16], and broadband detection [1]. These device properties can be attributed to the high absorption coefficient, suitable bandgap for photovoltaic application, and high electron mobility of TMDs [9, 17]. The p–n junction is the building block of photovoltaic SSPDs [18]. In the p–n junction-based SPPDs, the photo-generated electron/hole carriers can be separated by the built-in electric field at the interface of p-type and n-type 2D materials [19]. The p–n junction can be formed in a single 2D material using chemical doping [20] and double electrostatic gating [21]. However, creating a p–n homojunction with high stability using these methods is challenging and complicated [20, 22]. Alternatively, various p–n heterojunctions based on two different 2D materials, such as $WSe_2$, and other nanostructures can be fabricated by transfer techniques [23] with desirable band alignments and optoelectronic performance [1]. For instance, Chen *et al* [24] has reported a SPPD based on $WSe_2$/GaAs 2D/1D with a responsivity of ∼123 mA $W^{-1}$ at an incident light wavelength of 532 nm. A SPPD device with a maximum photoresponsivity of ∼100 mA $W^{-1}$ based on $WSe_2$/graphene 2D/2D structure has also been reported [25]. In another work, Zhang *et al* [26] has reported a broadband SPPD based on $WSe_2$/Si 2D/3D vertical heterojunction with a maximum photoresponsivity of 294 mA $W^{-1}$.

Zinc oxide (ZnO), an n-type semiconductor, is also a suitable material for UV photodetectors due to its wide band gap, high optical transmission, and fast switching time [27]. High-performance broadband photodetectors can be achieved by combining the photodetection performance of 2D TMD materials and ZnO nanostructures. For example, a 2D/1D heterostructure photodetector based on $MoSe_2$/ZnO nanorods with a responsivity of 330 mA $W^{-1}$ at a bias voltage of −2 V has been recently reported [28]. Moreover, a $MoSe_2$ (n-type)/ZnO (n-type) thin film heterostructure photodetector showed a fast photoresponse of 40 $\mu$s [27]. Nonetheless, the photodetection performance of a p–n heterojunction photodetector between a 2D material and thin film ZnO has not been explored yet.

Here, by taking advantage of a built-in electric field formed between p-type 2D $WSe_2$ and n-type ZnO thin film, a self-powered, broadband, and high-speed photodetector has been developed. To form the vertically stacked $WSe_2$/ZnO heterostructure, mechanically exfoliated $WSe_2$ was transferred on the ZnO thin film deposited by the atomic layer deposition (ALD) process. This structure shows a low dark current of ∼22 fA, a maximum photoresponsivity as high as ∼131 mA $W^{-1}$ and a specific detectivity of ∼3.92 × $10^{10}$ Jones under an incident light wavelength of $\lambda = 300$ nm at zero bias. It also shows a high cut-off frequency of ∼300 Hz with response rise/fall times of about ∼496/∼515 $\mu$s, making it suitable for high-speed self-powered optoelectronic applications. Under reverse bias, this photodetector demonstrates an ultrahigh steady-state responsivity of ∼7160 mA $W^{-1}$ and a high detectivity of ∼1.18 × $10^{11}$ Jones at −5 V bias voltage. Hence, the p-$WSe_2$/n-ZnO 2D/2D heterojunction is proposed as an excellent candidate for high-performance, self-powered, and broadband photodetectors.

## 2. Experimental section

### 2.1. Fabrication of the $WSe_2$/ZnO heterostructures

First, a uniform ZnO thin film with a thickness of ∼40 nm was deposited by ALD at a low deposition rate of ∼0.01 Å $S^{-1}$ at 130 °C on a Si substrate coated with 300 nm $SiO_2$ [29, 30]. The $SiO_2$/Si substrate was cleaned using a three-step cleaning with acetone, IPA, and DI water in bath sonication before the deposition. The deposited ZnO thin film was patterned into square shapes with sizes of 50 × 50 $\mu m^2$ through photolithography and etching processes. A diluted Hydrochloric acid (0.6 M HCl) was then used to etch the ZnO thin film and the additional photoresist was removed using acetone. 2D tungsten diselenide ($WSe_2$) flakes were mechanically exfoliated from a bulk $WSe_2$ crystal on a commercial PDMS film (Gel-Film, Gel-Pak) using a Nitto SPV224 tape [17, 31], then transferred on the patterned ZnO thin film using an all-dry deterministic stamping method using a micromanipulator [32]. The process was followed by heating at 100 °C for 5 min to increase the adhesion between ZnO thin film and the $WSe_2$ crystal. Subsequently, two Cr/Au (10/60 nm) electrode contacts were patterned by photolithography and deposited by thermal evaporation. The fabrication process is schematically shown in figure S1.

### 2.2. Material characterization

Field emission scanning electron microscopy (FESEM, FEI Nova NanoSEM 430) was used to observe the morphology of the sample. The thicknesses of ZnO thin film and $WSe_2$ flake were measured by an atomic force microscopy (AFM, Asylum MFP-3D) system. The ZnO and $WSe_2$ elemental compositions were determined using an energy dispersive x-ray analysis system.

### 2.3. Electrical/optical characterization

Electrical measurements were performed in a probe station connected to a Keithley (SCS 4200) semiconductor characterization system under ambient condition at room temperature. For the photodetection measurements, a monochromatic light with adjustable power generated by a solar simulator (Air Mass 1.5G spectrum) was directed to the $WSe_2$/ZnO device using a mirror and the electrical signals were collected using the Keithley system. An LED with a wavelength of 470 nm

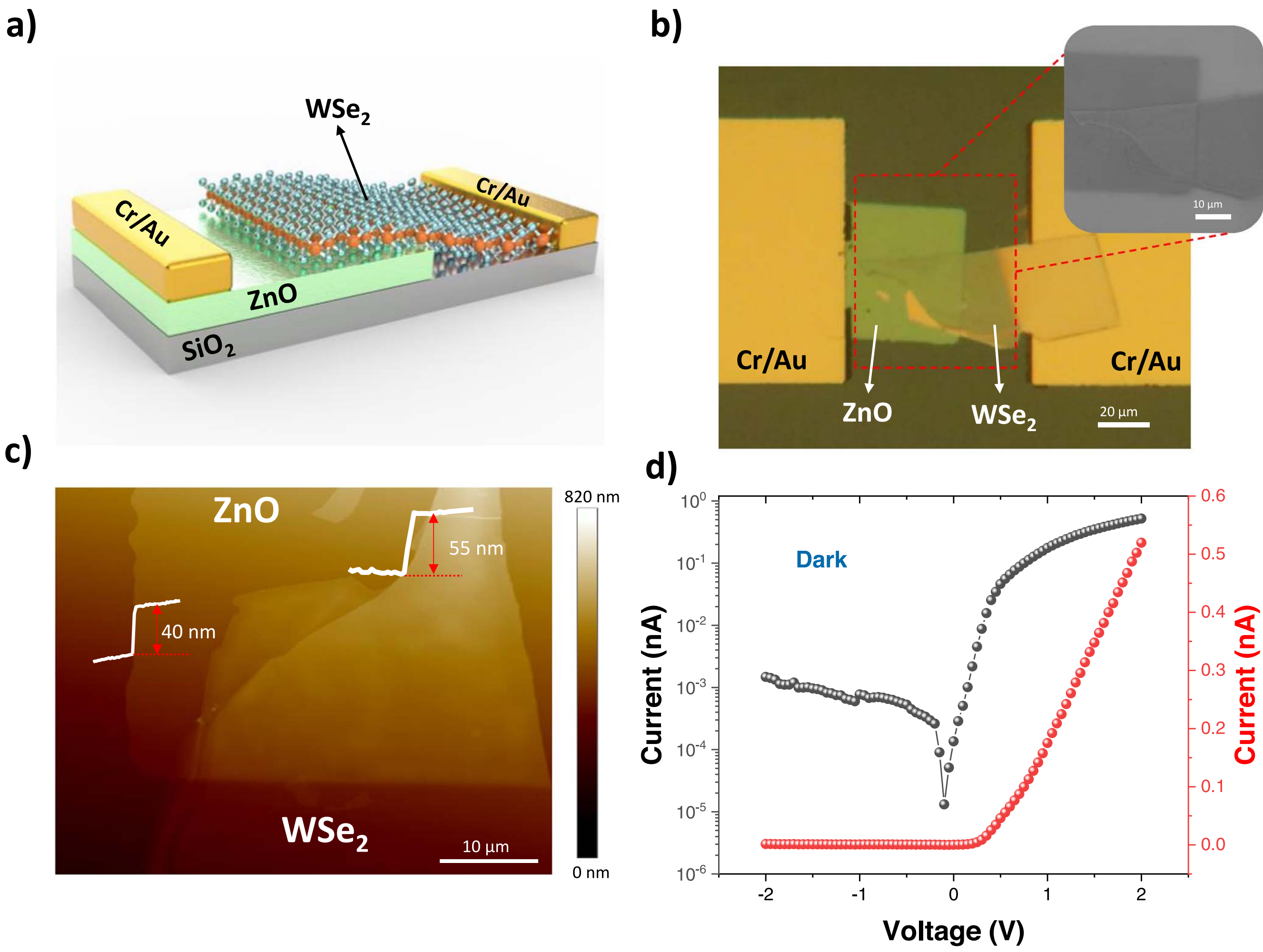


**Figure 1.** Structural and electrical characterization of the $WSe_2/ZnO$ heterostructure. (a) Schematic illustration of the $WSe_2/ZnO$ heterostructure device. (b) Optical microscopy image of the $WSe_2/ZnO$ heterostructure. The inset shows the SEM image of the $WSe_2/ZnO$ heterostructure. (c) AFM image of the $WSe_2/ZnO$ heterostructure, shows that the thickness of $WSe_2$ and ZnO are ∼55 nm and ∼40 nm, respectively. (d) The *I–V* characteristics of the $WSe_2/ZnO$ heterostructure under dark condition in the logarithmic (black) and linear (red) scales, show a current rectification of $\sim 10^3$ without a bias voltage.

connected to a function generator (Tektronix, AFG3151C) and an oscilloscope (Tektronix, MDO3104) were used to measure the frequency response of the $WSe_2/ZnO$ device as well as its response time. The rise time is defined as the time for the signal to increase from 10% to 90% of its final steady-state value, and the fall time is defined as the time for the signal to decrease from 90% to 10% of the steady-state value.

## 3. Results and discussion

A p-type $WSe_2$ crystal was transferred on the square shaped 40 nm thick n-type ZnO thin film. Two Cr/Au metal electrode contacts were deposited, one on the ZnO thin film and the other on the 2D $WSe_2$. Figure 1(a) shows the schematic illustration of the $WSe_2/ZnO$ heterostructure on the $SiO_2/Si$ substrate and the optical image of the fabricated $WSe_2/ZnO$ heterostructure is shown in figure 1(b). The contact area between $WSe_2$ and ZnO was calculated to be $\sim 637\ \mu m^2$. The scanning electron microscopy (SEM) image of the junction is also shown in the inset of figure 1(b). The energy dispersive x-ray spectroscopy was performed to confirm the elemental composition of ZnO and $WSe_2$ materials (figure S2). The thickness of multilayer $WSe_2$ flake and ZnO thin film are ∼55 nm and ∼40 nm, respectively, as determined by atomic force microscopy (AFM) (figure 1(c)). Monolayer $WSe_2$ has a direct bandgap, which makes it attractive for optoelectronic applications, but its low thickness hinders light absorption [33, 34]. In contrast, although multilayer $WSe_2$ has an indirect bandgap, the larger thickness can lead to high optical absorption with values approaching unity when coupled with a back reflector, making it suitable for photodetection applications [35]. The current–voltage (*I–V*) characteristic of the $WSe_2/ZnO$ heterojunction under dark condition is illustrated in figure 1(d), showing a high current rectification ratio, defined as the ratio of current at ±1 V, of $\sim 10^3$ without gate bias voltage. The diode rectification behavior can be attributed to the built-in electric field at the $WSe_2/ZnO$ interface [36]. Note that the Cr/Au electrode connected to the ZnO thin film is grounded during the *I–V* measurements.

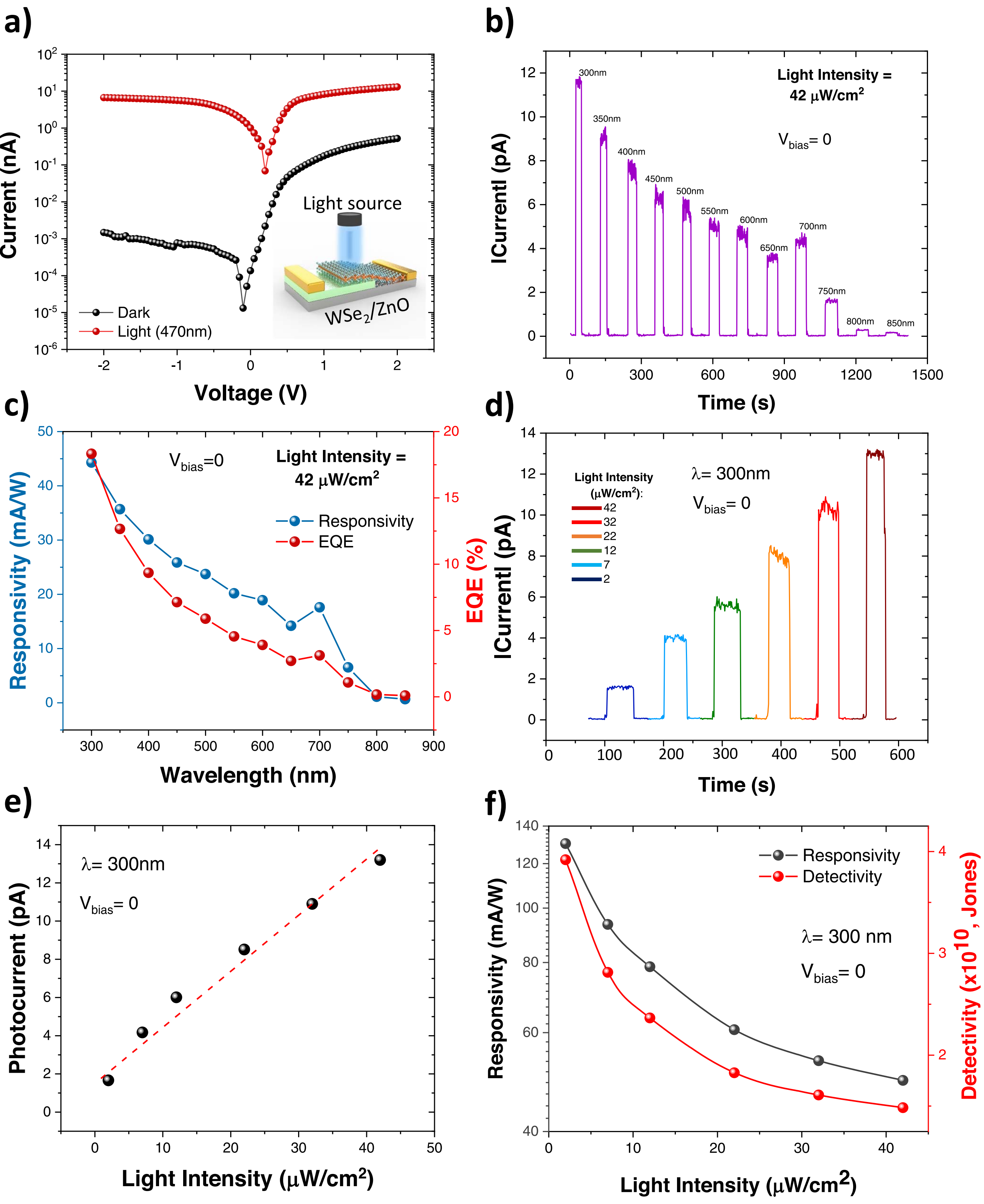


**Figure 2.** Self-powered photodetector characterization of the $WSe_2/ZnO$ heterojunction. (a) The *I–V* characteristics of the $WSe_2/ZnO$ heterojunction device under dark and light illumination ($\lambda = 470$ nm). Inset shows the device schematic under light illumination. (b) The *I–t* characteristics of the $WSe_2/ZnO$ heterojunction over a wide range of wavelengths ($\lambda = 300$–$850$ nm) at the same light intensity of 42 $\mu$W cm$^{-2}$ and zero bias voltage. (c) The responsivity and EQE over a wide range of wavelengths ($\lambda = 300$–$850$ nm) at the same light intensity of 42 $\mu$W cm$^{-2}$ and zero bias voltage. (d) The *I–t* characteristics of the $WSe_2/ZnO$ heterojunction over different light intensities (2–42 $\mu$W cm$^{-2}$) at the wavelength of $\lambda = 300$ nm and zero bias voltage. (e) The photocurrent amplitude at different light intensities (2–42 $\mu$W cm$^{-2}$). (f) The responsivity and detectivity of the $WSe_2/ZnO$ heterojunction as a function of light intensity (2–42 $\mu$W cm$^{-2}$).

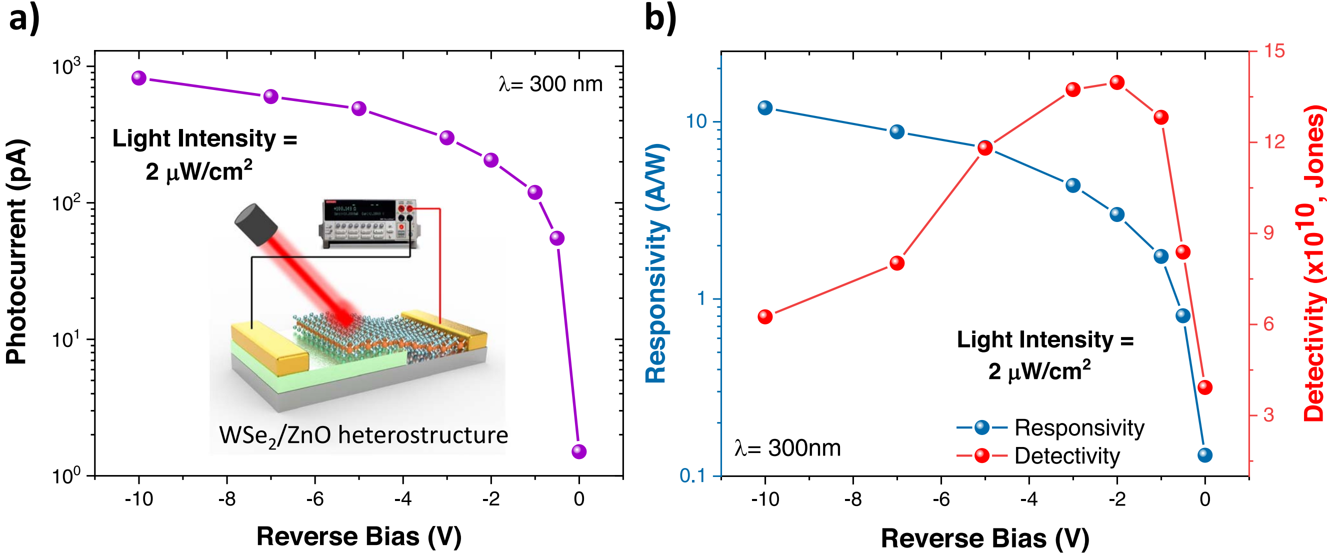


**Figure 3.** Photodetector characterization of the $WSe_2/ZnO$ heterojunction at several reverse bias voltages. (a) The photocurrent of the $WSe_2/ZnO$ heterojunction at several reverse bias voltages with the same light intensity of 2 $\mu$W cm$^{-2}$ and $\lambda = 300$ nm. Inset illustrates the schematic of the device under illumination at a reverse bias voltage. (b) The responsivity ($R$) and detectivity ($D^*$) of the photodetector at several reverse bias voltages with the same light intensity of 2 $\mu$W cm$^{-2}$ and $\lambda = 300$ nm.

The strong optical absorption of $WSe_2$ [37] in the visible-near-infrared ranges and ZnO at UV range [38] and the diode rectifying nature of the $WSe_2/ZnO$ heterojunction device makes it suitable for photodetection applications. The *I–V* characteristics of the $WSe_2/ZnO$ heterostructure device under dark and light illumination are demonstrated in figure 2(a). The current increases about four orders of magnitude upon light illumination at zero bias voltage (figure 2(a)) [4]. The self-powered collection of the photo-generated carriers at zero bias could be attributed to the strong built-in electric field at the $WSe_2/ZnO$ interface and the photovoltaic effect [39]. The inset of figure 2(a) shows the schematic illustration of the $WSe_2/ZnO$ heterojunction under light illumination. In figure 2(a), the photocurrent of ~0.01 $\mu$A at the light intensity of 1.5 mW cm$^{-2}$ and the device area of $S = 3480\ \mu m^2$, corresponds to a photocurrent density of ~300 $\mu$A cm$^{-2}$ for this device, which is relatively high compared to the previously reported 2D materials-based photodetectors [40, 41]. The small offset in the *I–V* characteristic at zero voltage may be due to the adsorption of oxygen and water molecules on the device surface [42, 43] or the existence of a parasitic capacitance in parallel with the device resistance [44]. Nevertheless, this deviation does not affect the performance of the device since the current–time (*I–t*) measurements show a constant dark current of ~22 fA without deviation. Figure S3 shows that the open-circuit voltage ($V_{oc}$) and short-circuit current ($I_{sc}$) of the $WSe_2/ZnO$ heterojunction device becomes as high as 350 mV and 15.6 nA, respectively, under UV light ($\lambda = 365$ nm) illumination at a light intensity of 4.58 mW cm$^{-2}$. A high $I_{photo}/I_{dark}$ ratio of $10^5$ was also measured using a light intensity of 4.58 mW cm$^{-2}$, which is higher than that of previously reported $WSe_2$-based heterojunctions [45, 46].

To evaluate the self-powered photodetection performance of the $WSe_2/ZnO$ device, the dynamic current–time (*I–t*) characteristics of the device was measured under monochromatic light illumination at different wavelengths ranging from $\lambda = 300$ to 850 nm, each with the same light intensity of 42 $\mu$W cm$^{-2}$, under zero bias voltage (figure 2(b)). The highest photocurrent of ~12 pA is achieved at $\lambda = 300$ nm, which is in agreement with the light absorption spectrum of $WSe_2$ and ZnO [37, 38]. The photoresponsivity and external quantum efficiency (EQE) of the $WSe_2/ZnO$ device under illumination over a wide range wavelength of $\lambda = 300$–850 nm are shown in figure 2(c). The maximum and minimum responsivities of 45 and 0.67 mA W$^{-1}$ are obtained at $\lambda = 300$ nm and 850 nm, respectively. Also, this photodetector has a responsivity of 17 mA W$^{-1}$, 6.54 mA W$^{-1}$, and 1.12 mA W$^{-1}$ at the wavelengths of 700, 750, and 800 nm. Despite its low responsivities in the 700–850 nm range, it is still classified as a broadband detector due to its ability to detect light across the UV (300–380 nm), visible (380–700 nm), and NIR (700–850 nm) spectra [4, 47]. The maximum EQE of ~18% was also achieved at $\lambda = 300$ nm at the light intensity of 42 $\mu$W cm$^{-2}$. The *I–t* characteristics of the $WSe_2/ZnO$ device at $\lambda = 300$ nm over several light intensities of ~2 to ~42 $\mu$W cm$^{-2}$ at zero bias are illustrated in figure 2(d). With increasing light intensity from 2 to 42 $\mu$W cm$^{-2}$, the photocurrent amplitude increases linearly (figure 2(e)), which is consistent with earlier findings [9, 10]. The photoresponsivity ($R$) and detectivity ($D^*$) of the $WSe_2/ZnO$ heterojunction versus light intensity at $\lambda = 300$ nm are shown in figure 2(f). Both responsivity and detectivity decrease as the light intensity increases which may be due to higher carrier recombination at higher light intensities [10]. The maximum photoresponsivity and detectivity are ~131 mA W$^{-1}$ and ~$3.92 \times 10^{10}$ Jones at the wavelength of $\lambda = 300$ nm with a light intensity of ~2 $\mu$W cm$^{-2}$ at zero bias. The EQE was also calculated to be ~54.3% at the lowest light intensity of ~2 $\mu$W cm$^{-2}$, which is much higher than the EQE of ~18% at the highest light intensity of ~42 $\mu$W cm$^{-2}$.

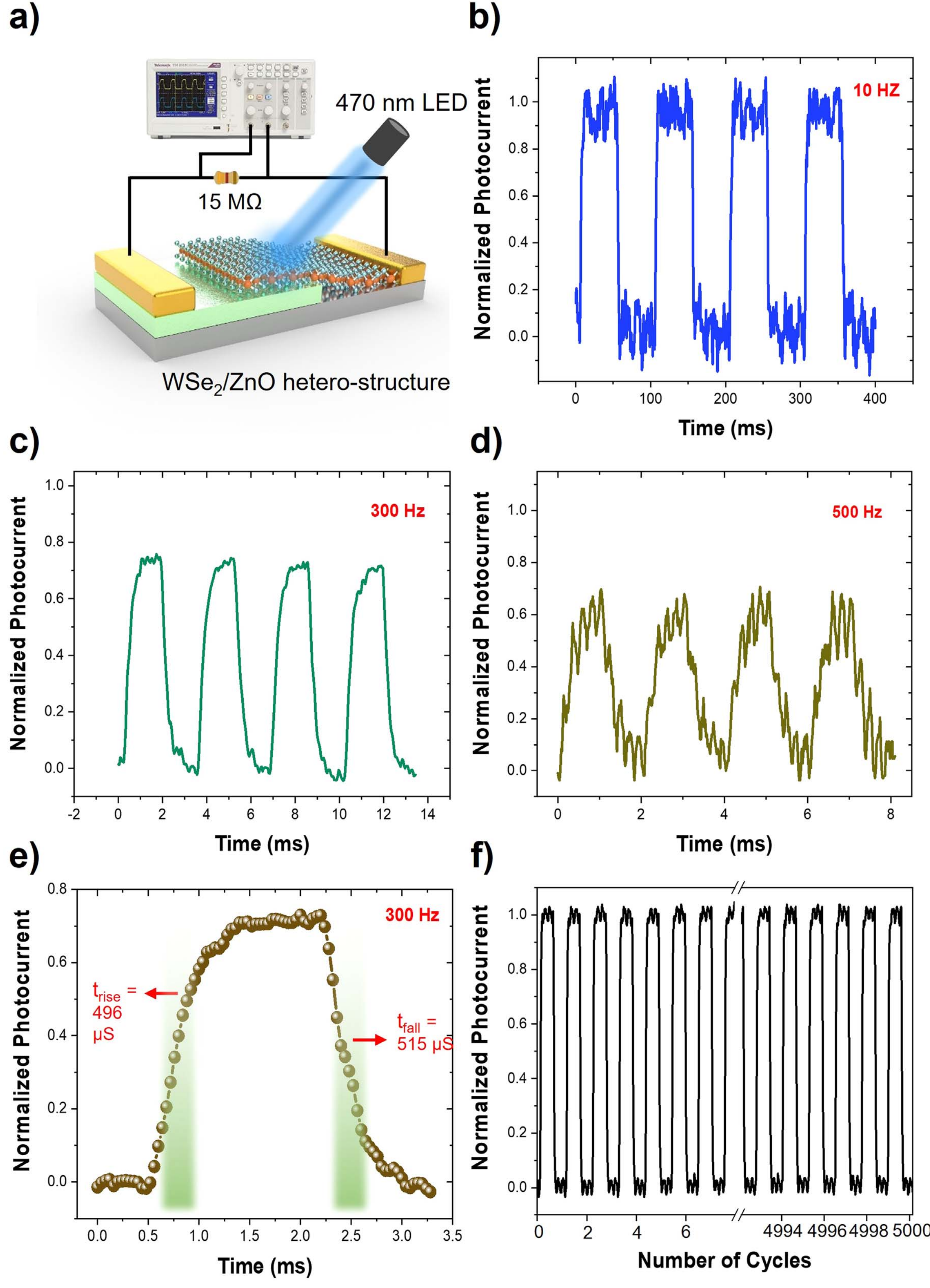


**Figure 4.** The frequency-dependent photoresponse of the $WSe_2/ZnO$ heterojunction device. (a) Schematic of the setup for dynamic response measurements. Normalized photocurrent of the $WSe_2/ZnO$ device with zero applied voltage under the optical pulses with $\lambda = 470$ nm and frequencies of (b) 10 Hz, (c) 300 Hz, and (d) 500 Hz. (e) Single normalized photocurrent signal at the frequency of 300 Hz. The rise and fall times are 496 $\mu$s and 515 $\mu$s, respectively. (f) The stability test of the $WSe_2/ZnO$ device over 5000 consecutive optical pulses ($\lambda = 470$ nm) at zero bias voltage.

**Table 1.** Performance evaluation of the $WSe_2/ZnO$ photodetector in comparison to other $WSe_2$- and ZnO-based photodetectors in terms of the device structure, bias voltage, wavelength ($\lambda$), maximum responsivity ($R_{max}$), rise/fall times ($t_{rise}/t_{Fall}$), and maximum detectivity ($D^*_{max}$).

| Device structure | Self-powered | $\lambda$ (nm) | $R_{max}$ (mA $W^{-1}$) | $t_{rise}$ | $t_{fall}$ | $D^*_{max}$ (Jones) | References |
|---|---|---|---|---|---|---|---|
| $WSe_2$/Graphite | No (1 V) | 390–1080 | 6.66 | 0.8 (S) | 1.4 (S) | $1.98 \times 10^8$ | [56] |
| $WSe_2$ monolayer | No (1 V) | 400–1400 | 360 | 310 (mS) | 930 (mS) | $1 \times 10^9$ | [57] |
| $WSe_2$/graphene/$MoTe_2$ | Yes (0 V) | 350/1050 | 40.84 | 468 ($\mu$S) | 428 ($\mu$S) | $1.2 \times 10^{11}$ | [45] |
| $WSe_2/MoTe_2$ | Yes (0 V) | 400–1700 | 1.8 | 72 ($\mu$S) | 48 ($\mu$S) | — | [46] |
| $WSe_2/MoSe_2$ | Yes (0 V) | 375–811 | 100 | 1.25 (mS) | 1.5 (mS) | $5.78 \times 10^{15}$ | [58] |
| $WSe_2/MoSe_2$ | No (−2 V) | 1550 | 127 | | | — | [59] |
| $MoTe_2$/Si | Yes (0 V) | 400–1550 | 260 | 5 ($\mu$S) | 8 ($\mu$S) | $2 \times 10^{13}$ | [60] |
| $MoS_2$/Si | Yes (0 V) | 450–1050 | 210 | 3 ($\mu$S) | 40 ($\mu$S) | $1 \times 10^{13}$ | [61] |
| $MoSe_2$/Si | Yes (0 V) | 405–2500 | 522 | 18 ($\mu$S) | 10 ($\mu$S) | $6.7 \times 10^9$ | [62] |
| ZnO film | No (30 V) | 200–400 | 67.08 | — | — | — | [63] |
| ZnO/Si | No (4 V) | 200–500 | 360 | 11 (S) | 14 (S) | — | [64] |
| ZnO/Se film | Yes (0 V) | 300–600 | 2.65 | 0.69 (mS) | 13.5 (mS) | — | [65] |
| $WSe_2$/ZnO | Yes (0 V) | | 131 | 496 ($\mu$S) | 515 ($\mu$S) | $3.92 \times 10^{10}$ | |
| | No (−2 V) | 300–850 | 2995 | | | $1.39 \times 10^{11}$ | **This Work** |
| | No (−5 V) | | 7160 | | | $1.18 \times 10^{11}$ | |
| | No (−10 V) | | 11983 | | | $6.2 \times 10^{10}$ | |

The observation of the higher EQE at low incident light intensity than at high light intensity has also been shown in $WSe_2$ photodetectors [48]. The peak in responsivity and EQE at $\lambda = \sim 700$ nm could be attributed to the excitonic absorption peak in $WSe_2$ [49, 50]. The dark current of this photodetector device is also remarkably low, ~22 fA, which may be suppressed by the depletion region at the $WSe_2$/ZnO interface [51]. The main photodetector parameters including responsivity ($R$), detectivity ($D^*$), and EQE values were calculated using the equations (1)–(4) [52, 53].

$$I_{ph} = I_{light} - I_{dark} \quad (1)$$

$$R = |I_{ph}/(P \times S)| \quad (2)$$

$$\mathrm{EQE} = \frac{hcR}{e\lambda} \quad (3)$$

$$D^* = \frac{S^{1/2}R}{(2eI_{dark})^{1/2}}, \quad (4)$$

where $I_{ph}$, $I_{dark}$, and $I_{light}$ are the photocurrent, dark current and current under illumination, respectively; $P$ is the light intensity and $S$ is the effective surface area and $h$, $c$, $e$, and $\lambda$ are Planck's constant, speed of light, electron charge constant, and wavelength, respectively [52].

To investigate the collection/separation of photo-generated carriers under different reverse voltage conditions, the photocurrent was measured under several reverse bias voltages at a constant light intensity of 2 $\mu$W $cm^{-2}$ and the wavelength of $\lambda = 300$ nm. Figure 3(a) shows the amplitude of the generated photocurrent under reverse bias voltages of 0, −0.5, −1, −2, −3, −5, −7, and −10 V. A schematic illustration of the measurement setup is shown in the inset of figure 3(a). Small reverse bias voltages (e.g. −0.5 V and −1 V) result in a significant increase in photocurrent due to the facilitation of charge collection. The effect of reverse bias on photocurrent nearly saturates at values $\geqslant -5$ V (figure 3(a)) [4, 54]. The maximum photoresponsivity of 11.98 A $W^{-1}$ was obtained at the voltage bias of −10 V (figure 3(b)). Note that both dark current and photocurrent increase with increasing reverse bias voltage (figure S4). The responsivities of 1.74, 2.99, 4.37, 7.16, and 8.77 A $W^{-1}$ were achieved for the reverse biases of −1, −2, −3, −5, and −7 V, respectively (figure 3(b)), which are much higher than the responsivity at the zero bias (0.131 A $W^{-1}$). Interestingly, as the applied reverse bias voltage across the $WSe_2$/ZnO heterojunction increases, the responsivity increases sublinearly but the detectivity increases up to the peak value of $\sim 1.39 \times 10^{11}$ Jones at −2 V and thereafter decreases with further increase in applied reverse bias voltage [55]. The detectivity highly depends on the responsivity and the dark current of the device (equation (4)). At the bias voltages higher than −2 V, the dark current increase rate is surpassing the responsivity growth rate, resulting in a decrease in detectivity. Therefore, the optimum performance of the $WSe_2$/ZnO photodetector is at a reverse bias voltage of −2 V. The EQE of the device increases significantly to a value of ~4958% at the bias voltage of −10 V (figure S5). The EQE cannot exceed 100% at zero bias without photomultiplication [4]. With the help of the reverse bias, the EQEs can enhance to values much higher than 100% due to the photoconductivity gain effect [4]. Note that the whole device area ($S$ = 3480 $\mu m^2$) is considered active for the calculation of the responsivities/detectivities at the non-zero bias voltages.

The self-powered frequency-dependent photoresponse of the $WSe_2$/ZnO photodetector was investigated in figure 4. A 470 nm LED powered by a function generator was used to generate light pulses with different frequencies and the $WSe_2$/ZnO device was connected to an oscilloscope through a resistor (15 M$\Omega$) to measure the time-dependent photocurrent (figure 4(a)). The normalized $I$–$t$ characteristics of the device with zero applied voltage under the light frequencies of 10, 300, and 500 Hz are shown in figure (b)–(d), respectively. The

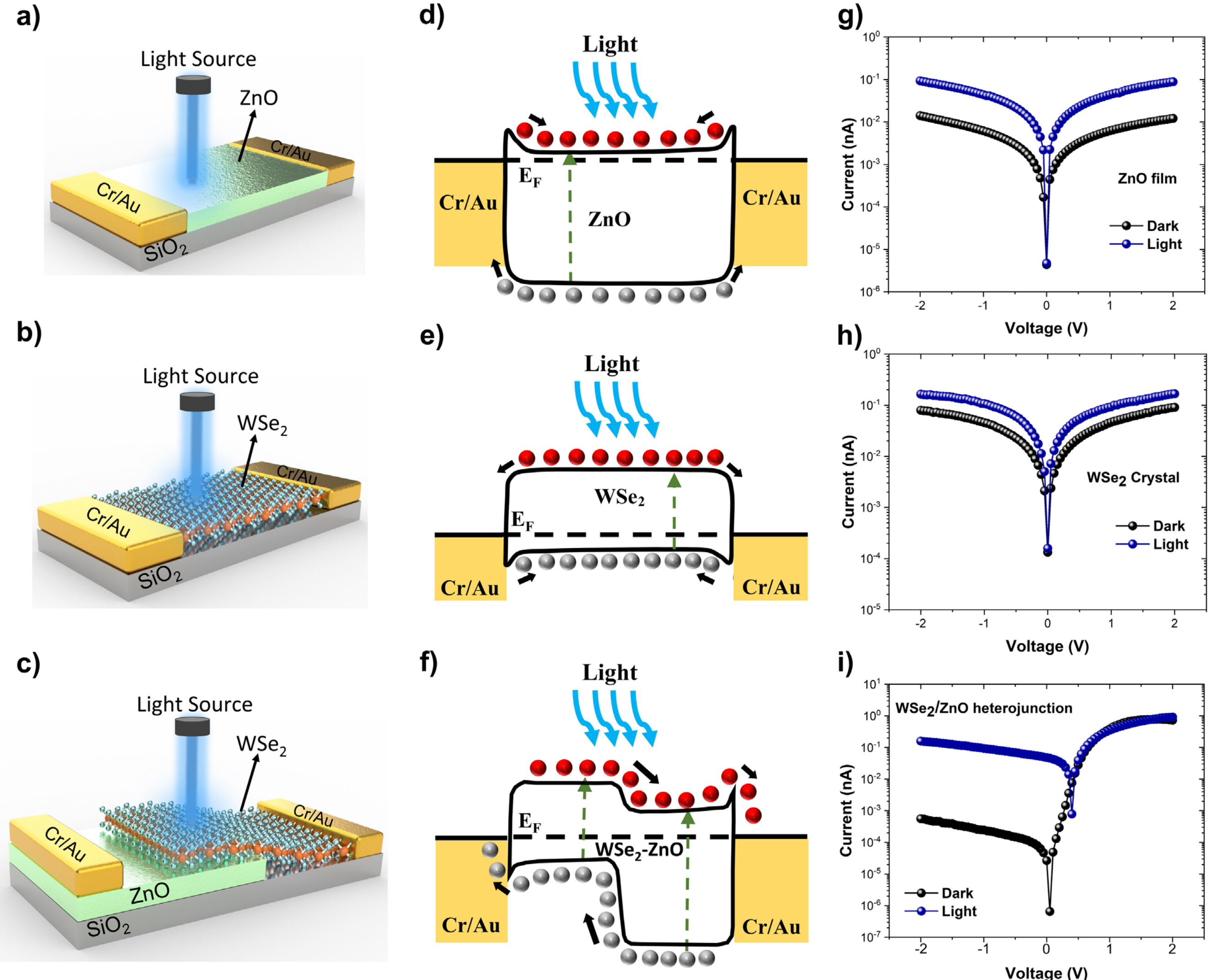


**Figure 5.** Working mechanism of the $WSe_2/ZnO$ heterojunction. The schematic of (a) the Cr-ZnO-Cr device, (b) the Cr-$WSe_2$-Cr device, and (c) the $WSe_2/ZnO$ heterojunction device. The energy band diagram of (d) the Cr-ZnO-Cr device, (e) the Cr-$WSe_2$-Cr device, and (f) the $WSe_2/ZnO$ heterojunction device. The *I–V* characteristics of (g) the Cr-ZnO-Cr device, (h) the Cr-$WSe_2$-Cr device, and (i) the $WSe_2/ZnO$ heterojunction device under dark and light conditions.

normalized photoresponses in frequencies of 50, 150, and 800 Hz are also illustrated in figures S6(a)–(c). The photocurrent amplitude as a function of light frequency is shown in figure S6(d), illustrating a cut-off frequency of ~300 Hz. The amplitude of the photoresponse at 300 Hz is about ~0.74 which is about 70% of its maximum value at the frequency of 1 Hz. At higher frequencies, the photocurrent amplitude drops significantly. The cut-off frequency is the frequency at which the amplitude of the photocurrent signal drops by a factor of 70% [4]. The response time and fall times of ~496 and ~515 $\mu$s were measured for a square wave optical input signal with a frequency of 300 Hz (figure 4(e)), demonstrating the suitability of this device for fast self-powered optoelectronic applications. Figure 4(f) illustrates the stability of the photoresponse of the $WSe_2/ZnO$ photodetector over 5000 consecutive light pulses, showing a square wave photoresponse without a notable degradation in the signal amplitude.

The photodetection performance of the recently published 2D $WSe_2$- and ZnO-based photodetectors is compared to our $WSe_2/ZnO$ heterojunction photodetector in table 1. The $WSe_2/ZnO$ heterojunction photodetector is broadband, highly responsive, fast, and offers high responsivities and detectivities, compared to the previous works listed in table 1. The responsivity of the $WSe_2/ZnO$ device under reverse bias voltages is almost two orders of magnitudes higher than those of other $WSe_2$- and ZnO-based photodetectors.

To investigate the mechanism of the self-powered photodetection in the $WSe_2/ZnO$ heterojunction, three devices based on the ZnO thin film, $WSe_2$ crystal, and $WSe_2/ZnO$ heterojunction were fabricated. The schematic of the Cr-ZnO-Cr, Cr-$WSe_2$-Cr, and Cr-$WSe_2$/ZnO-Cr structures under light illumination are shown in figures 5(a)–(c), respectively. Figures 5(d)–(f) illustrate the energy band diagram of the devices under light illumination. The electron affinity of ZnO

is ~4.3–4.5 eV [66] and the work function of Cr is ~4.5 eV [9], resulting in two equal Schottky barriers with the Cr electrodes (figure 5(d)) [67]. These equal Schottky barriers lead to a net photocurrent of about zero (~5 fA) at zero bias when the device is under light illumination (figure 5(g)) [9, 68]. However, the photocurrent is non-zero when applying a bias voltage to the device due to the separation of carriers by the applied electric field [69]. Similarly, the $WSe_2$ crystal, with an electron affinity of ~4 eV [70] and a work function of ~4.8 eV [71], forms two equal Schottky barriers with Cr electrodes (figure 5(e)) [71], which results in a net photocurrent of about zero (~0.03 pA) when the whole device is under light illumination (figure 5(h)). This small photocurrent could be due to the unwanted $WSe_2$/Cr contact area asymmetry at two electrodes [9, 72]. Therefore, the symmetric metal-semiconductor-metal device structure is not suitable for SSPD application [9]. However, when contacting the $WSe_2$ and ZnO, a built-in electric field is formed at the interface due to the energy band bending, leading to a high current rectification ratio of $\sim 10^3$ under dark conditions and a large net photocurrent (~45 pA) under light illumination with zero bias (figure 5(i)). Therefore, the high $V_{oc}$ = ~400 mV and $I_{sc}$ = ~45 pA in the $WSe_2$/ZnO heterojunction is attributed to the presence of a strong built-in electric field at the $WSe_2$/ZnO interface and the separation/acceleration of electron/hole carriers by the electric field in the depletion region [73]. The ideality factor ($n$) and barrier height ($\phi_B$) of the $WSe_2$/ZnO diode are calculated to be $n$ = ~2.83 and $\phi_B$ = ~0.87 $V$ (Section I, Supporting Information), which are comparable to the previously reported ZnO/Si heterostructure diode [74].

One important consideration for SPPDs is large-area scalability. In this work, the $WSe_2$ flakes were mechanically exfoliated and transferred on the patterned ZnO thin film to demonstrate proof-of-concept $WSe_2$/ZnO photodetection devices. The ZnO thin film is scalable to large areas by ALD and large area 2D materials can be prepared by chemical vapor deposition (CVD) [75] or wet chemical processes [76]. Therefore, it is possible to scale up this proof-of-concept photodetector to an imaging array of $WSe_2$/ZnO photodetectors on a chip. Hence, the fast response, broadband detection, high-speed, and high responsivity of the $WSe_2$/ZnO heterostructure make it an excellent candidate for self-powered optoelectronic applications.

## 4. Conclusion

A self-powered broadband photodetector based on p-$WSe_2$ and n-ZnO thin film was developed. The $WSe_2$/ZnO p–n heterojunction photodetector showed a broadband response (300–850 nm) with maximum responsivity and detectivity of ~131 mA $W^{-1}$ and ~3.92 × $10^{10}$ Jones under $\lambda$ = 300 nm at zero bias, respectively. The responsivity and detectivity of the device increase to ~7160 mA $W^{-1}$ and ~1.18 × $10^{11}$ Jones, respectively, under a reverse bias voltage of −5 V, which is due to the facilitation of charge collection under bias voltage. The photodetector also exhibited a cut-off frequency of ~300 Hz, a fast response time of ~496 $\mu$s, and a remarkable photocurrent stability over 5000 light pulse cycles. Hence, the p-$WSe_2$/n-ZnO based photodetector is a candidate for self-powered, high-speed, and broadband photodetection technology.

## Acknowledgments

This work was supported by the Natural Sciences and Engineering Research Council of Canada (NSERC), Canada Foundation for Innovation (CFI), British Columbia Knowledge Development Fund (BCKDF), Western Economic Diversification Canada (WD), and Simon Fraser University. The authors thank B Kim for maintenance of the SFU Engineering Science cleanroom facility. The authors acknowledge CMC Microsystems and 4D LABS shared facilities that facilitated this research.

## Data availability statement

The data cannot be made publicly available upon publication because they are not available in a format that is sufficiently accessible or reusable by other researchers. The data that support the findings of this study are available upon reasonable request from the authors.

## ORCID iDs

Amin Abnavi https://orcid.org/0000-0002-9458-9957
Thushani De Silva https://orcid.org/0000-0002-5377-0952
Michael M Adachi https://orcid.org/0000-0003-3015-2606

## References

[1] Long M, Wang P, Fang H and Hu W 2019 *Adv. Funct. Mater.* **29** 1803807
[2] Zhou H, Lai H, Sun X, Zhang N, Wang Y, Liu P, Zhou Y and Xie W 2022 *ACS Appl. Mater. Interfaces* **14** 3356–62
[3] Cao F, Yan T, Li Z, Wu L and Fang X 2022 *Adv. Opt. Mater.* **10** 2200786
[4] Ahmadi R, Abnavi A, Ghanbari H, Mohandes H, Mohammadzadeh M R, De Silva T, Hasani A, Fawzy M, Kabir F and Adachi M M 2022 *Nano Energy* **98** 107285
[5] Tai G, Liu B, Hou C, Wu Z and Liang X 2021 *Nanotechnology* **32** 505606
[6] Su L, Yang W, Cai J, Chen H and Fang X 2017 *Small* **13** 1701687
[7] Li S, Guo D, Li P, Wang X, Wang Y, Yan Z, Liu Z, Zhi Y, Huang Y and Wu Z 2019 *ACS Appl. Mater. Interfaces* **11** 35105–14
[8] Anbarasan N *et al* 2023 *Nanotechnology* **34** 135201
[9] Abnavi A, Ahmadi R, Ghanbari H, Fawzy M, Hasani A, De Silva T, Askar A M, Mohammadzadeh M R, Kabir F and Whitwick M 2022 *Adv. Funct. Mater.* **33** 2210619
[10] Hasani A, Mohammadzadeh M R, Ghanbari H, Fawzy M, Silva T D, Abnavi A, Ahmadi R, Askar A M, Kabir F and Rajapakse R 2022 *ACS Omega* **7** 48383–90

[11] Wen Z, Fu J, Han L, Liu Y, Peng M, Zheng L, Zhu Y, Sun X and Zi Y 2018 *J. Mater. Chem.* C **6** 11893–902

[12] Liu X-L, Zhao Y, Wang W-J, Ma S-X, Ning X-J, Zhao L and Zhuang J 2020 *IEEE Sens. J.* **21** 5628–44

[13] Mohammadzadeh M R, Hasani A, Jaferzadeh K, Fawzy M, De Silva T, Abnavi A, Ahmadi R, Ghanbari H, Askar A and Kabir F 2023 *Advanced Science* (Germany: Weinheim, Baden-Wurttemberg) e2205458

[14] Zhu Y, Raj V, Li Z, Tan H H, Jagadish C and Fu L 2021 *Adv. Mater.* **33** 2105729

[15] Ghasemi F, Abdollahi A, Abnavi A, Mohajerzadeh S and Abdi Y 2018 *IEEE Electron Device Lett.* **39** 1465–8

[16] Tang W, Liu C, Wang L, Chen X, Luo M, Guo W, Wang S-W and Lu W 2017 *Appl. Phys. Lett.* **111** 153502

[17] Abnavi A, Ahmadi R, Hasani A, Fawzy M, Mohammadzadeh M R, De Silva T, Yu N and Adachi M M 2021 *ACS Appl. Mater. Interfaces* **13** 45843–53

[18] Li D, Chen M, Sun Z, Yu P, Liu Z, Ajayan P M and Zhang Z 2017 *Nat. Nanotechnol.* **12** 901–6

[19] Pedapudi M C and Dhar J C 2022 *Nanotechnology* **33** 255203

[20] Choi M S, Qu D, Lee D, Liu X, Watanabe K, Taniguchi T and Yoo W J 2014 *ACS nano* **8** 9332–40

[21] Frisenda R, Molina-Mendoza A J, Mueller T, Castellanos-Gomez A and Van Der Zant H S 2018 *Chem. Soc. Rev.* **47** 3339–58

[22] Tsai M L, Li M Y, Retamal J R D, Lam K T, Lin Y C, Suenaga K, Chen L J, Liang G, Li L J and He J H 2017 *Adv. Mater.* **29** 1701168

[23] Watson A J, Lu W, Guimarães M H and Stöhr M 2021 *2D Mater.* **8** 032001

[24] Chen X, Jiang B, Wang D, Li G, Wang H, Wang H, Wang F, Wang P, Liao L and Wei Z 2021 *Appl. Phys. Lett.* **118** 041102

[25] Chen R, Liu G, Qiu F, Tan Y and Chen F 2022 *Opt. Mater. Express* **12** 3614–20

[26] Zhang X, Shao J, Su Y, Wang L, Wang Y, Wang X and Wu D 2022 *Ceram. Int.* **48** 29722–9

[27] Wan Z, Mu H, Dong Z, Hu S, Yu W, Lin S and Mokkapati S 2021 *Mater. Des.* **212** 110185

[28] Jana S, Pal S, Bhaktha S B and Ray S K 2022 *ACS Appl. Nano Mater.* **5** 18106–15

[29] Jeon S, Bang S, Lee S, Kwon S, Jeong W, Jeon H, Chang H J and Park H-H 2008 *J. Electrochem. Soc.* **155** H738

[30] Krajewski T A, Terziyska P, Luka G, Lusakowska E, Jakiela R, Vlakhov E S and Guziewicz E 2017 *J. Alloys Compd.* **727** 902–11

[31] Yarrow B, Askar A M, Parameswaran A M and Adachi M M 2019 *ACS Appl. Electron. Mater.* **1** 2150–6

[32] Askar A M, Saeed M, Hamed A, Negra R and Adachi M M 2021 *Nanoscale* **13** 8940–7

[33] Yang C-x, Zhao X and Wei S-y 2016 *Solid State Commun.* **245** 70–4

[34] Jariwala D, Davoyan A R, Tagliabue G, Sherrott M C, Wong J and Atwater H A 2016 *Nano Lett.* **16** 5482–7

[35] Tian H, Chin M L, Najmaei S, Guo Q, Xia F, Wang H and Dubey M 2016 *Nano Res.* **9** 1543–60

[36] Zhu Q, Ye P, Tang Y, Zhu X, Cheng Z, Xu J and Xu M 2021 *Nanotechnology* **33** 115202

[37] Dong N, Li Y, Feng Y, Zhang S, Zhang X, Chang C, Fan J, Zhang L and Wang J 2015 *Sci. Rep.* **5** 1–10

[38] Patil V L, Vanalakar S A, Patil P S and Kim J H 2017 *Sensors Actuators* B **239** 1185–93

[39] Sun Y, Hu R, An C, Ma X, Zhang J and Liu J 2021 *Nanotechnology* **32** 475206

[40] Liu Y, Lu C, Luo M, Han T, Ge Y, Dong W, Xue X, Zhou Y and Xu X 2022 *Nanoscale Horiz.* **7** 1217–27

[41] Ansari R M, Salunke A D, Rahil M and Ahmad S 2023 *Adv. Mater. Interfaces* **10** 2202170

[42] Jeon P J, Min S-W, Kim J S, Raza S R A, Choi K, Lee H S, Lee Y T, Hwang D K, Choi H J and Im S 2015 *J. Mater. Chem.* C **3** 2751–8

[43] Abnavi A, Ahmadi R, Ghanbari H, Fawzy M, Hasani A, De Silva T, Askar A M, Mohammadzadeh M R, Kabir F and Whitwick M 2023 *Adv. Funct. Mater.* **33** 2210619

[44] Wu G, Wang X, Wang P, Huang H, Chen Y, Sun S, Shen H, Lin T, Wang J and Zhang S 2016 *Nanotechnology* **27** 364002

[45] Feng P, He S, Zhao S, Dang C, Li M, Zhao L, Lu H-L and Gao L 2022 *J. Mater. Chem.*C **10** 9401–6

[46] Chen J, Shan Y, Wang Q, Zhu J and Liu R 2020 *Nanotechnology* **31** 295201

[47] Sharma M, Aggarwal P, Singh A, Kaushik S and Singh R 2022 *ACS Appl. Nano Mater.* **5** 13637–48

[48] Zhou C, Raju S, Li B, Chan M, Chai Y and Yang C Y 2018 *Adv. Funct. Mater.* **28** 1802954

[49] Ezgi Eroglu Z, Contreras D, Bahrami P, Azam N, Mahjouri-Samani M and Boulesbaa A 2021 *Nanomaterials* **11** 770

[50] Su G, Gao A, Peng B, Hu J, Zhang Y, Liu F, Zhang H, Zhan P and Wu W 2022 *Nanophotonics* **11** 3149–57

[51] Gao W, Zhang S, Zhang F, Wen P, Zhang L, Sun Y, Chen H, Zheng Z, Yang M and Luo D 2021 *Adv. Electron. Mater.* **7** 2000964

[52] Wu E, Wu D, Jia C, Wang Y, Yuan H, Zeng L, Xu T, Shi Z, Tian Y and Li X 2019 *ACS photon.* **6** 565–72

[53] Ejehi F, Shooshtari L, Mohammadpour R, Asadian E and Sasanpour P 2022 *Nanotechnology* **33** 475205

[54] Ma D, Wang R, Zhao J, Chen Q, Wu L, Li D, Su L, Jiang X, Luo Z and Ge Y 2020 *Nanoscale* **12** 5313–23

[55] Mukherjee S, Maiti R, Katiyar A K, Das S and Ray S K 2016 *Sci. Rep.* **6** 1–11

[56] Pataniya P M and Sumesh C 2020 *Synth. Met.* **265** 116400

[57] Hu C, Dong D, Yang X, Qiao K, Yang D, Deng H, Yuan S, Khan J, Lan Y and Song H 2017 *Adv. Funct. Mater.* **27** 1603605

[58] Kim J E, Kang W T, Kim Y R, Shin Y S, Lee I, Won U Y, Lee B H, Kim K, Phan T L and Lee Y H 2021 *J. Mater. Chem.* C **9** 3504–12

[59] Xue H, Wang Y, Dai Y, Kim W, Jussila H, Qi M, Susoma J, Ren Z, Dai Q and Zhao J 2018 *Adv. Funct. Mater.* **28** 1804388

[60] Lei W, Cao G, Wen X, Yang L, Zhang P, Zhuge F, Chang H and Zhang W 2021 *Appl. Phys. Lett.* **119** 131902

[61] Wang L, Jie J, Shao Z, Zhang Q, Zhang X, Wang Y, Sun Z and Lee S T 2015 *Adv. Funct. Mater.* **25** 2910–9

[62] John J W, Dhyani V, Maity S, Mukherjee S, Ray S K, Kumar V and Das S 2020 *Nanotechnology* **31** 455208

[63] Tian C, Jiang D, Zhao Y, Liu Q, Hou J, Zhao J, Liang Q, Gao S and Qin J 2014 *Mater. Sci. Eng.* B **184** 67–71

[64] Al-Hardan N, Jalar A, Hamid M A, Keng L K, Ahmed N and Shamsudin R 2014 *Sensors Actuators* A **207** 61–6

[65] Hu K, Teng F, Zheng L, Yu P, Zhang Z, Chen H and Fang X 2017 *Laser Photon. Rev.* **11** 1600257

[66] Liu Z, Liu Y, Wang X, Li W, Zhi Y, Wang X, Li P and Tang W 2019 *J. Appl. Phys.* **126** 045707

[67] Gao J, Liu W-J, Ding S-J, Lu H-L and Zhang D W 2018 *AIP Adv.* **8** 015015

[68] Li H, Xu P, Liu D, He J, Zu H, Song J, Zhang J, Tian F, Yun M and Wang F 2021 *Nanotechnology* **32** 375202

[69] Mahmoodi E, Amiri M H, Salimi A, Frisenda R, Flores E, Ares J R, Ferrer I J, Castellanos-Gomez A and Ghasemi F 2022 *Sci. Rep.* **12** 12585 (https://nature.com/articles/s41598-022-16834-8)

[70] Liu B, Tang B, Lv F, Zeng Y, Liao J, Wang S and Chen Q 2019 *Nanotechnology* **31** 065203
[71] Wang H, Gao W, Wen P, Yu H, Huang Y, Yue Q, Wang X and Huo N 2022 *Adv. Electron. Mater.* **8** 2200649
[72] De Silva T, Fawzy M, Hasani A, Ghanbari H, Abnavi A, Askar A, Ling Y, Mohammadzadeh M R, Kabir F and Ahmadi R 2022 *Nat. Commun.* **13** 7593
[73] Gu J *et al* 2022 *Nanotechnology* **33** 405402
[74] Faraz S M, Shah W, Alvi N U H, Nur O and Wahab Q U 2020 *Adv. Condens. Matter Phys.* **2020** 1–9
[75] Baek S H, Choi Y and Choi W 2015 *Nanoscale Res. Lett.* **10** 1–6
[76] Hasani A, Van Le Q, Tekalgne M, Choi M-J, Choi S, Lee T H, Kim H, Ahn S H, Jang H W and Kim S Y 2019 *ACS Appl. Mater. Interfaces* **11** 29910–6